ROYAL SOCIETY OF CHEMISTRY

PAPER

Check for updates

High precision selenium isotope analysis using a Nu Sapphire collision–reaction cell MC-ICP-MS

Michael A. Kipp, [ID] *[a] Laura F. Piccirillo [ID] [a] and Daniel Peters[b]

Selenium is a redox-sensitive trace element that is both an essential nutrient and toxin. Studying selenium cycling in nature is of great interest to the fields of environmental health, geomicrobiology, chemical oceanography and volcanology. The six stable isotopes of selenium are fractionated during redox reactions, leaving fingerprints of redox conditions and micronutrient dynamics in modern and ancient environments. However, the study of selenium isotope variability in nature is plagued by analytical difficulties, including its low natural abundance and the prevalence of argon-based interferences in plasma-based mass spectrometers. Here we present a new approach to selenium isotopic analysis using a collision–reaction cell multiple collector inductively coupled plasma mass spectrometer. By using a He–N$_2$ gas mixture, we can achieve near-complete removal of argon dimers from the beam, allowing precise analysis of all selenium isotopes. This new method enables greater analytical precision per nanogram of selenium analyzed and is also less sensitive to concentration mismatch between samples and standards. Future work can leverage CRC-equipped mass spectrometers to study subtle isotopic effects in low-selenium reservoirs.

1. Introduction

Selenium (Se) is a chalcophilic trace element.[1] It is both an essential micronutrient and a toxin at fairly low concentration.[2–4] At Earth's surface, Se occupies multiple oxidation states (Se^{-II}, Se^0, Se^{IV}, Se^{VI}), with the oxidized species forming the soluble oxyanions selenite (SeO$_3^{2-}$) and selenate (SeO$_4^{2-}$). Reduction of Se oxyanions generates elemental Se^0 and inorganic selenide (Se^{-II}), the latter of which can substitute for sulfur in sulfide minerals.

Studying the cycling of Se in surface environments is important for tracking contaminant transport.[5,6] Furthermore, the proportions of Se in various valence states can provide information about environmental redox conditions in present or past environments.[7–9] Stable isotope ratios provide a useful means of tracking these transitions between redox states, as Se has six stable isotopes (Table 1) that experience mass-dependent fractionation during redox reactions.[10–13] Over the past few decades, several studies have explored the potential of Se isotope geochemistry to track environmental pollution,[14–16] paleo-redox conditions,[17–23] hydrothermal systems[24–26] and solar system formation.[27,28]

Despite its promise as a biogeochemical tracer, analysis of Se isotopes faces multiple hurdles. First, Se is present at low levels in geological (~60 ng g^{-1} in crust[29,30]) and aqueous

($\leq$160 ng L^{-1} in ocean[31]) samples. Second, Se is volatile, and losses during sample preparation can induce substantial isotopic fractionation.[32] Third, and most importantly for this study, Se analysis *via* multiple collector inductively coupled plasma mass spectrometry (MC-ICP-MS) is plagued by isobaric interference from argon dimers (^{74}ArAr, ^{76}ArAr, ^{78}ArAr, ^{80}ArAr; Table 1). This typically means that ^{80}Se, the most abundant isotope (49.8%), cannot be resolved from ^{80}ArAr (mass resolution of >20 000 would be required) or adequately corrected, and thus half of the potential Se signal cannot be analyzed. Interferences on ^{78}Se, ^{76}Se and ^{74}Se can also increase analytical uncertainty if not properly corrected.[33,34]

Collision–reaction cell (CRC) equipped MC-ICP-MS instruments have the potential to eliminate Ar-based interferences, enabling more sensitive and precise Se isotopic analysis. By introducing gases to the ion flight path that collide or react with ArAr, the abundance of ArAr relative to an analyte of interest (in this case, Se) can be reduced by orders of magnitude. While some early work on Se isotopes used a CRC-MC-ICP-MS (Micromass Isoprobe), most applications[35,36] used Ar in the cell and thus did not explore ArAr signal reduction *via* collision or reactions with other gases. Furthermore, the Isoprobe never became widespread and most MC-ICP-MS method development over the past few decades has used non-CRC approaches. In the last few years, a new generation of CRC-MC-ICP-MS instrumentation has emerged (Nu Sapphire and Thermo Neoma), raising the possibility of again exploring CRC-MC-ICP-MS analysis of Se isotopes. If successful, this approach could potentially improve the precision of ^{74}Se, ^{76}Se, ^{78}Se and ^{80}Se

[a]Division of Earth and Climate Sciences, Nicholas School of the Environment, Duke University, Durham, NC, 27708, USA. E-mail: michael.kipp@duke.edu

[b]Nu Instruments Ltd, Wrexham LL13 9XS, UK

Paper   JAAS

Table 1 Selenium isotopes and their major isobaric interferences. Mass dispersion is $\frac{1}{2}$ for Nu detector array

Detector	L6	L5	L4	L2	Ax	H2	H4	H5	H6	H7	H8	
Mass (amu)	73	74	75	76	77	78	79	80	81	82	83	84
Selenium		^{74}Se (0.86%)		^{76}Se (9.23%)	^{77}Se (7.60%)	^{78}Se (23.7%)		^{80}Se (49.8%)		^{82}Se (8.82%)		
Se hydrides			^{74}SeH		^{76}SeH	^{77}SeH	^{78}SeH		^{80}SeH		^{82}SeH	
Argon		^{36}Ar^{38}Ar		^{36}Ar^{40}Ar; ^{38}Ar^{38}Ar		^{38}Ar^{40}Ar		^{40}Ar^{40}Ar				
Ar hydrides					^{36}Ar^{40}ArH; ^{38}Ar^{38}ArH		^{38}Ar^{40}ArH		^{40}Ar^{40}ArH			
Germanium	^{73}Ge (7.76%)	^{74}Ge (36.5%)		^{76}Ge (7.8%)								
Ge hydrides		^{73}GeH	^{74}GeH		^{76}GeH							
Arsenic			^{75}As (100%)									
As hydrides				^{75}AsH								
Krypton						^{78}Kr (0.4%)		^{80}Kr (2.3%)		^{82}Kr (11.6%)	^{83}Kr (11.5%)	^{84}Kr (57.0%)
Kr hydrides							^{78}KrH		^{80}KrH		^{82}KrH	^{83}KrH

analyses while simultaneously reducing sample requirements and enabling monitoring of all isotope pairs for thorough assessment of mass-dependent behavior. Given the scarcity of Se in most natural samples, these would be important analytical advances.

Here we describe protocols for Se isotope analysis using a Nu Sapphire CRC-MC-ICP-MS. We compare protocols with and without the collision–reaction cell, employing published interference correction schemes.[33,34] We find that the Sapphire is capable of high-precision Se isotope analyses in both the high-energy (non-CRC) and low-energy (CRC) modes. Analyses employing the CRC can match the external reproducibility of non-CRC analyses using ~40% less Se. This will help to reduce Se requirements for sample-limited analyses, and also allows a broader survey of all Se isotopes for precise exploration of mass-independent isotopic effects.

2. Experimental

2.1 Sample preparation

All lab work was conducted in GAIA Lab (Geoscience Applications of Isotopic Analysis) in the Division of Earth and Climate Sciences at Duke University. Unless otherwise specified, all acids were twice-distilled from ACS reagent grade acid or purchased as Optima grade.
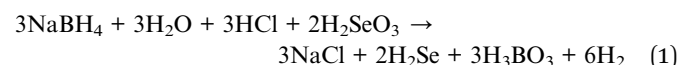
A geostandard, USGS Cody Shale (SCo-1; Split #7, Position #4), was prepared for isotopic analysis to allow comparison to published work. Sample powders (~0.5 g) were digested in a 1 : 1 : 1 combination of concentrated HF, HNO$_3$ and HClO$_4$ at 130 °C for two days. Digests were dried to incipient dryness, and additional HClO$_4$ was added to ensure complete digestion of organic matter. Final digests were dried to incipient dryness, reconstituted in 2 mL of 5.5 M HCl, capped and refluxed at 100 °C for one hour to allow reduction of Se^{VI} to Se^{IV}. After cooling, the solutions were diluted to 0.5 M HCl.

Selenium was purified from digests using thiol-silica resin.[37] Columns (6 mL bed volume, 250 μL resin volume; Phenomenex) were cleaned with 0.5 M HCl before loading samples in 0.5 M HCl and subsequently washing the matrix through the column with additional 0.5 M HCl. Selenium was eluted from the columns by conversion from Se^{IV} to Se^{VI} using 15 M HNO$_3$. The purified Se fraction was dried to a ~500 μL drop and 1.5 mL of 11 M HCl was added to form aqua regia. This solution was dried at 55 °C to a ~250 μL drop, reconstituted in 1 mL 6 M HCl, capped and refluxed at 100 °C for one hour to convert Se^{VI} to Se^{IV}. The solution was then diluted to 0.5 M HCl for isotopic analysis. Procedural blanks were <1 ng Se and column yields were consistently >90% for solution and rock standards.

2.2 Sample introduction

Sample solutions were introduced to the Sapphire using a hydrideICP (Elemental Scientific, Inc.) hydride generation system. Prior work has demonstrated that hydride generation significantly improves Se ionization yields;[35] we observed that moving from standard wet plasma (cyclonic glass spray chamber, 0.3 M HNO$_3$ solution) to the hydride generator (HG) increased transmission by a factor of >300, similar to what has been observed by others.[38]

The HG uses sodium borohydride (NaBH$_4$, 1 wt% in 0.01 M NaOH) as a reductant and HCl (here 0.5 M) as the run acid, facilitating the reaction:

$$3NaBH_4 + 3H_2O + 3HCl + 2H_2SeO_3 \rightarrow 3NaCl + 2H_2Se + 3H_3BO_3 + 6H_2 \quad (1)$$

Salt accumulation in the HG required regular (~daily) rinsing to prevent blockage of gas transmission to the mass spectrometer, as noted by ref. 34 using the same HG model. The HG peristaltic pump was operated at 20–40 rpm (typically 25), which corresponded to uptake rates of ~467 μL min^{-1} for sample solution, ~237 μL min^{-1} for NaBH$_4$ solution, and ~117

µL min^{-1} for additional 0.5 M HCl. A single analysis (80 s uptake time followed by 50 cycles of 4 s each), therefore consumed ~2.2 mL of sample solution.

2.3 High-energy path: Se isotopic analysis without collision–reaction cell

The Sapphire possesses two ion flight paths: a "high-energy" path for non-CRC analyses, and a "low-energy" path for CRC analyses (Fig. 1), with "low-energy" referring to the lower kinetic energies of the ions in the collision–reaction cell (Table 2). Initial analytical tests were performed using the high-energy path to replicate prior work using previous-generation MC-ICP-MS instruments (Nu Plasma 1, 2 and 3; Thermo Neptune and NeptunePlus). Typical operating parameters for the high-energy mode are given in Table 2. For these analyses, the instrument was operated in low mass resolution mode and peak centering was performed on each sample, standard and blank analysis. Tuning was performed as-needed (~daily) to maintain maximal signal intensity, stability and peak alignment (Fig. 2A).

2.4 Low-energy path: incorporation of the collision–reaction cell

Following establishment of high-energy path protocols, analyses were performed using the low-energy path. Typical tuning parameters are given in Table 2. Cell gas mixtures of He–H$_2$ and He–N$_2$ were explored, following prior work.[39,40] Using He–N$_2$, an unknown polyatomic interference was occasionally observed on mass 80 at a level of up to a few mV (Fig. 2B). This could represent ^{40}Ar^{16}O^{23}NaH, ^{35}Cl^{16}O^{28}N$_2$H, or another combination of elements present in the HG solutions or cell gases. Because the interference was easily resolved from ^{80}Se, we performed measurements in low resolution on the interference-free peak shoulder using the "delta M" method in the Nu software to specify the distance from the low-mass half-intensity to the point at which to measure.

2.5 Data reduction

All isotopic ratios are reported in delta notation relative to NIST SRM 3149 (Lot #992106):

$$\delta^{82/xx}\mathrm{Se} = \left(\frac{^{82/xx}\mathrm{Se_{sample}}}{^{82/xx}\mathrm{Se_{NIST\text{-}3149}}} - 1 \right) \times 1000 \qquad (2)$$

Table 2 Typical tuning parameters

	High-energy (non-CRC)	Low-energy (CRC)
Plasma		
Coolant gas	13.0 L min^{-1}	13.0 L min^{-1}
Auxiliary gas	0.8 L min^{-1}	0.8 L min^{-1}
Nebulizer pressure	4.0 psi	4.0 psi
RF power	1300 W	1300 W
Acceleration	6000 V	4000 V
Extraction	3500 V	2000 V
Collision cell		
He	N/A	0–1 mL min^{-1}
H$_2$	N/A	0 mL min^{-1}
N$_2$	N/A	1–2 mL min^{-1}
Hydride generator		
Sample uptake	467 µL min^{-1}	467 µL min^{-1}
NaBH$_4$ uptake	237 µL min^{-1}	237 µL min^{-1}
HCl uptake	117 µL min^{-1}	117 µL min^{-1}
Pump speed	25 rpm	25 rpm

Isotope ratios were corrected using both standard-sample bracketing and isotope dilution. A new ^{74}Se–^{77}Se double spike (DS) solution was prepared using pure ^{74}Se and ^{77}Se solutions (IsoFlex). The optimal DS composition and DS : sample ratio were determined following Rudge et al.[41] and using the code from Klaver and Coath[42] (Fig. 3A). The optimal values (Fig. 3A) are similar to those determined using the Double Spike Toolbox[41] (^{77}Se/^{74}Se = 0.93; DS/(DS + sample) = 0.37), but differ slightly because following Klaver and Coath,[42] we allowed for non-fixed sample voltage, as has been noted by others[43,44] to be important for sample-limited measurements. The DS composition was calibrated via analyses of mixtures with NIST SRM 3149 and validated with analyses of mixtures with MH-495, a pure Se solution used in prior work[18,32,45] (Fig. 3B). We note that while other Se double spikes have been explored that enable similar or even slightly superior analytical precision,[32,34,46] the choice to spike the least abundant Se isotopes (^{74}Se and ^{77}Se) allows the greatest improvement in counting statistics while not saturating detectors (as pointed out by ref. 43). Thus, the ^{74}Se–^{77}Se spike is best suited for precise isotopic analysis of low-Se materials. Furthermore, while spiking on top of major interferences can be advantageous,[43] in this case the major interferent (^{80}ArAr) occurs on the major Se isotope, leaving little room for spiking before detector saturation.
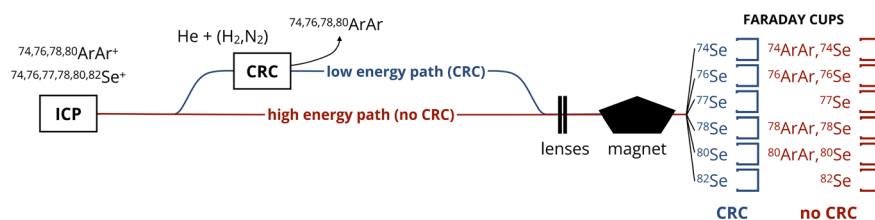

Fig. 1 Ion flight path in Nu Sapphire MC–ICP-MS. Only argon dimer interferences are shown; additional isobaric interferences that are not removed by the CRC are shown in Table 1.
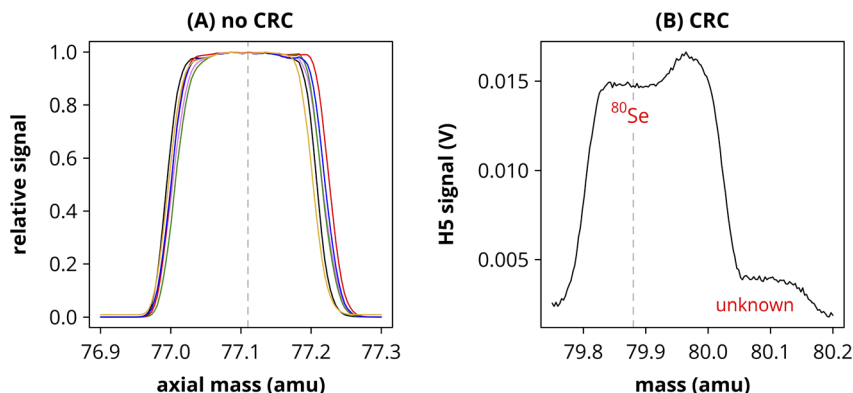
2794 | J. Anal. At. Spectrom., 2025, **40**, 2792–2802

This journal is © The Royal Society of Chemistry 2025

Fig. 2 Peak scans in (A) non-CRC and (B) CRC measurement modes. Measurements in both modes are performed in low mass resolution. Peak centering is performed for non-CRC analyses, while a low-mass peak shoulder analysis is performed for CRC analyses to avoid unknown polyatomic interferences on the high-mass shoulder. Dashed lines illustrate mass used for isotopic analyses.

We monitored masses 73 to 83 using faraday cups coupled to amplifiers with 10^{11} Ω resistors, where a single measurement consisted of 50 cycles lasting 4 s each of integration time. Drawing on prior work,[33,34] Se beam intensities were corrected for isobaric interferences in the manner outlined below. Following correction for isobaric interferences, delta values were calculated using both standard-sample bracketing (SSB) and double spike (DS) deconvolution. Since the system is over-constrained – four isotopic ratios (five when including ^{80}Se), three unknowns – a least-squares regression was used to find the optimal solution to the double spike equations.

2.5.1 Krypton. The signal measured on mass 83 in the on-peak zero (OPZ; 0.5 M HCl) was assumed to derive overwhelmingly from ^{83}Kr, as the ^{82}SeH signal should be well below detection (see hydride rates below). The ^{82}Kr, ^{80}Kr and ^{78}Kr contributions to the subsequent sample or standard analysis were thus determined by multiplying by the Kr natural abundance (NA):

$$^{82,80,78}\text{Kr} = {}^{83}\text{Kr}_{meas}({}^{82,80,78}\text{Kr}/{}^{83}\text{Kr})_{NA} \quad (3)$$

These inferred Kr signals (typically $\leq$0.5 mV for ^{82}Kr) were subtracted from the sample and standard signals. We note that this Kr contribution is not corrected for instrumental mass bias, but due to the small magnitude of the correction the impact on isotopic ratios is negligible.

2.5.2 Argon. To correct Ar dimer interferences, we followed Stüeken et al.[33] in using the clean ^{82}Se signal (after Kr correction as above) to calculate a predicted ^{80}Se signal using natural Se isotopic abundances[47] $[({}^{80}\text{Se}/{}^{82}\text{Se})_{NA} = 5.647027]$. The ^{80}ArAr signal was then estimated as the difference between the measured signal on mass 80 and that predicted from ^{80}Se:

$$^{80}\text{ArAr} = {}^{80}\text{Se}_{meas} - {}^{82}\text{Se}_{corr}({}^{80}\text{Se}/{}^{82}\text{Se})_{NA}e^{\beta \cdot \log(m80/m82)} \quad (4)$$

where β is the instrumental mass bias factor and mXX denotes the respective absolute isotopic mass. The instrumental mass bias was estimated:

$$\beta = (({}^{82}\text{Se}_{corr}/{}^{78}\text{Se}_{corr})/({}^{82}\text{Se}/{}^{78}\text{Se})_{NA})/\log(m82/m78) \quad (5)$$

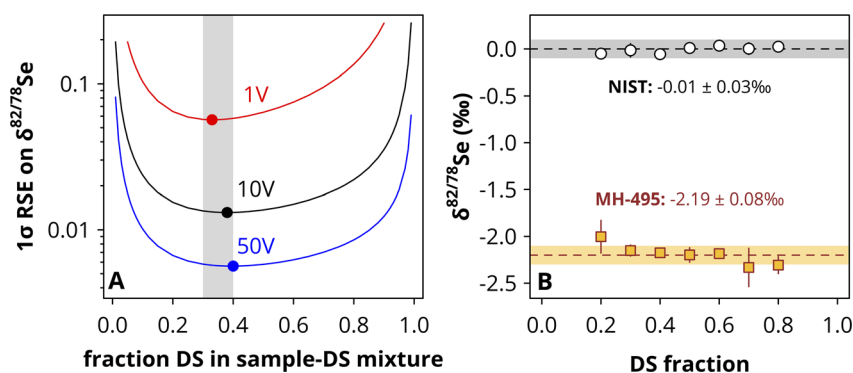We note that inaccuracies in mass bias estimation will not significantly impact these corrections, as even using

Fig. 3 Double spike (A) composition and (B) calibration. Theoretical precision limits were calculated for a ^{74}Se–^{77}Se spike at various spiking ratios using the approach of Klaver and Coath.[42] Across the range of sample intensities expected for typical analyses (1–50 V total Se signal), the optimal spiking ratio is 30–40% (grey shaded area). Our ^{74}Se–^{77}Se spike was calibrated using NIST SRM 3149 and validated via analyses of MH-495, which yielded values consistent with published data for spiking ratios from 20% to 80%.

This journal is © The Royal Society of Chemistry 2025

J. Anal. At. Spectrom., 2025, **40**, 2792–2802 | **2795**

unfractionated natural isotopic abundance has a negligible (<0.01‰) impact on corrected isotopic ratios in most cases. This ^{80}ArAr signal was then used to calculate ^{76}ArAr and ^{78}ArAr contributions using natural isotopic abundances (^{76}ArAr/^{80}ArAr = 0.006636; ^{78}ArAr/^{80}ArAr = 0.001257):

$$^{78,76}\text{ArAr} = {}^{80}\text{ArAr}({}^{78,76}\text{ArAr}/{}^{80}\text{ArAr})_{\text{NA}} \quad (6)$$

Mass bias correction was not applied to Ar dimer abundances, since the impact would be even smaller than the already negligible correction on the ^{80}Se signal estimation. The calculated ^{76}ArAr (80–100 mV) and ^{78}ArAr (15–20 mV) contributions were then subtracted from the observed mass 76 and 78 signals (contributions from ^{74}ArAr were <0.07 mV and thus ignored). For non-CRC analyses, the ^{80}Se signal was not used for SSB or DS delta value calculations. For CRC analyses, ^{80}Se was included, but no ArAr corrections were applied due to near-complete removal of ArAr interferences and adequate correction from OPZ subtraction.

2.5.3 Selenium hydrides. Selenium hydride rates were determined using the signal measured on mass 83 in the sample and standard analyses:

$$\text{SeH rate} = {}^{82}\text{SeH}_{\text{meas}}/{}^{82}\text{Se}_{\text{corr}} \quad (7)$$

After subtracting the ^{83}Kr contribution from the OPZ, a ^{82}SeH signal of 1–4 mV was typically observed, corresponding to ^{82}SeH/^{82}Se hydride rates of <10^{-3} on average. The determined hydride rate was used to calculate and subtract contributions from ^{77}SeH and ^{76}SeH on masses 78 and 77, respectively:

$$^{77,76}\text{SeH} = {}^{77,76}\text{Se}_{\text{corr}}\ (\text{SeH rate}) \quad (8)$$

2.5.4 Argon hydrides. The ArArH rate was determined using the signal on mass 81 in sample and standard analyses. The contribution from ^{80}SeH was estimated using the predicted ^{80}Se signal as above and the Se hydride rate. The ^{80}SeH contribution was then subtracted, yielding the ^{80}ArArH signal. The ArArH rate was estimated as:

$$\text{ArArH rate} = ({}^{80}\text{ArArH}_{\text{meas}} - {}^{80}\text{Se}_{\text{corr}}\ (\text{SeH rate}))/{}^{80}\text{ArAr} \quad (9)$$

This rate was used to determine the ^{76}ArArH contribution to subtract from the mass 77 signal:

$$^{76}\text{ArArH} = {}^{76}\text{ArAr}\ (\text{ArArH rate}) \quad (10)$$

2.5.5 Germanium. The signal from germanium (Ge) was determined by monitoring mass 73 during sample and standard measurements. The ^{73}Ge signal was then used to calculate ^{74}Ge and ^{76}Ge signals. For small Ge corrections – as in the correction schemes described above – using natural isotopic abundances (^{74}Ge/^{73}Ge = 4.706186; ^{76}Ge/^{73}Ge = 0.9987113) was accurate; however, for large Ge corrections (approaching Ge/Se ~1), it was necessary to account for instrumental mass fractionation when scaling the ^{73}Ge signal to ^{74}Ge and ^{76}Ge

intensities. We did this by calculating the mass bias factor (β) using Se isotopes as in eqn (5). The Ge interferences were then calculated as:

$$^{76,74}\text{Ge} = {}^{73}\text{Ge}_{\text{meas}}\ ({}^{76,74}\text{Ge}/{}^{73}\text{Ge})_{\text{NA}}\ e^{\beta \cdot \log(m76,74/m73)} \quad (11)$$

We also estimated and subtracted the ^{73}GeH contribution to ^{74}Se using the SeH rate:

$$^{73}\text{GeH} = {}^{73}\text{Ge}_{\text{meas}}\ (\text{SeH rate}) \quad (12)$$

2.5.6 Arsenic. Arsenic (As) has a single stable isotope, ^{75}As, which does not directly interference with any Se isotopes. However, ^{75}AsH can interfere on ^{76}Se and so this was monitored and subtracted. The ^{75}As signal at mass 75 was determined after subtracting the contributions from ^{74}SeH and ^{74}GeH. The Se hydride rate was then used to estimate the ^{75}AsH signal, which was subtracted from the signal on mass 76:

$$^{75}\text{AsH} = ({}^{75}\text{As}_{\text{meas}} - {}^{74}\text{SeH} - {}^{74}\text{GeH})\ (\text{SeH rate}) \quad (13)$$

2.5.7. Summary

Accounting for all isobaric interference corrections described above, the final corrected Se signals were calculated as follows:

$$^{82}\text{Se}_{\text{corr}} = {}^{82}\text{Se}_{\text{meas}} - {}^{82}\text{Kr} \quad (14)$$

$$^{80}\text{Se}_{\text{corr}} = {}^{80}\text{Se}_{\text{meas}} - {}^{80}\text{ArAr} - {}^{80}\text{Kr} \quad (15)$$

$$^{78}\text{Se}_{\text{corr}} = {}^{78}\text{Se}_{\text{meas}} - {}^{78}\text{ArAr} - {}^{78}\text{Kr} - {}^{77}\text{SeH} \quad (16)$$

$$^{77}\text{Se}_{\text{corr}} = {}^{77}\text{Se}_{\text{meas}} - {}^{76}\text{SeH} - {}^{76}\text{ArArH} \quad (17)$$

$$^{76}\text{Se}_{\text{corr}} = {}^{76}\text{Se}_{\text{meas}} - {}^{76}\text{ArAr} - {}^{76}\text{Ge} - {}^{75}\text{AsH} \quad (18)$$

$$^{74}\text{Se}_{\text{corr}} = {}^{74}\text{Se}_{\text{meas}} - {}^{74}\text{Ge} - {}^{73}\text{GeH} \quad (19)$$

4. Results and discussion

4.1 Sensitivity and precision in high- and low-energy paths

We first consider the sensitivity of our analyses under different operating conditions. Given the Se-limited nature of many studies, we aimed to optimize Se transmission and signal intensity. We used a hydride generator to produce H$_2$Se to improve ionization efficiency. We found that varying HCl molarity of the sample and supplementary acid from 0.5 M to 2.0 M produced a <10% change in signal intensity and SeH rates, with greater intensity associated with higher relative SeH rates. We therefore opted to use 0.5 M HCl for our run acid to minimize hydride formation, be less corrosive, and conserve acid. Under typical tuning, we could achieve 2.5–3.0 V on ^{82}Se for a 50 ppb solution in the high-energy (non-CRC) path (560–670 V total unspiked Se signal per ppm), which is greater than or comparable to prior work.[32–34]

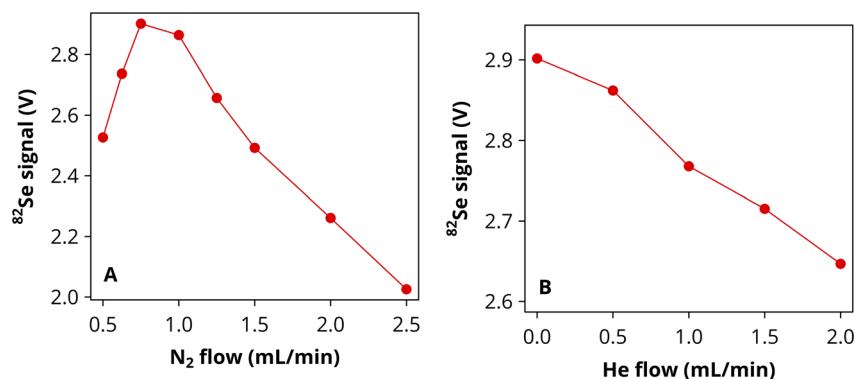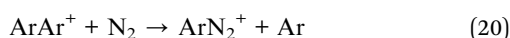2796 | J. Anal. At. Spectrom., 2025, **40**, 2792–2802

This journal is © The Royal Society of Chemistry 2025

Fig. 4 Selenium signal as function of (A) N_2 and (B) He cell gases. Signal intensity is maximized with moderate (0.8 to 1.0 mL min^{-1}) N_2 flow and minimal He flow into the collision reaction cell.

For analyses employing the low-energy (CRC) path, we tested two different cell gas combinations. First, following recent method development using a Nu Sapphire[40] and based on prior work,[39] we tested a He–N_2 mixture. Using N_2 as a reaction gas is known to reduce the signal from ArAr$^+$ ions *via* a ligand exchange reaction:[39,48]

$$ArAr^+ + N_2 \rightarrow ArN_2^+ + Ar \tag{20}$$

We found that when using a He–N_2 cell gas mixture (or N_2 alone), with optimal tuning in the low-energy (CRC) path we could match the same sensitivity as non-CRC analyses, typically by minimizing He flow and using an N_2 flow rate of 0.8 to 1.0 mL min^{-1} (Fig. 4). Under these conditions, on-peak zero measurements of 0.5 M HCl gave a signal of 10–20 mV on the low-mass shoulder of mass 80 (Fig. 2B) and an ^{80}Se/^{78}Se ratio of ~2. Given that this nearly matches the natural ^{80}Se/^{78}Se ratio (~2.1) and is much lower than the ^{80}ArAr/^{78}ArAr ratio (~800), we infer that there is a negligible contribution from ArAr$^+$ ions to any measured beam intensities when using N_2 in the CRC.

We also tested He–H_2 mixtures. While similar Se signal sensitivity could be achieved as with He–N_2 mixtures, the SeH rate increased to as high as 3%, more than an order of magnitude greater than with He–N_2 (<0.1%). As a result, even when employing SeH corrections, the precision of isotope ratio measurements worsened (Fig. 5). Thus, we opted to use He–N_2 rather than He–H_2 in our CRC analyses.

We next consider the analytical precision of isotope ratio measurements. To assess the controls on internal precision, we followed prior work[41–43,49–52] in calculating the theoretical contributions to measurement uncertainty from Johnson–Nyquist noise (σ_{Johnson}) and counting statistics (σ_{counting}):

$$\sigma_{\text{Johnson}} = \sqrt{\frac{4kTt}{e^2 R}} \tag{21}$$

$$\sigma_{\text{counting}} = \sqrt{\frac{1}{n_{\text{eff}}}} \tag{22}$$

where k is the Boltzmann constant, T is the detector temperature, t is the integration time, e is the elementary charge, and R is the amplifier resistance. The parameter n_{eff} is defined[50] as

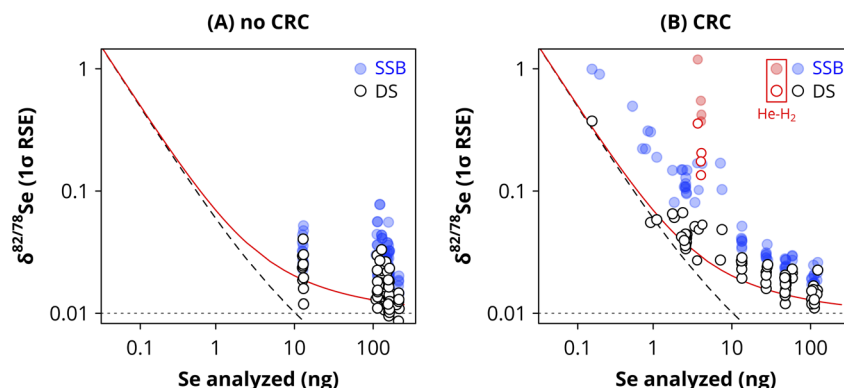$$n_{\text{eff}} = n_a n_b (n_a + n_b) \tag{23}$$

Fig. 5 Demonstration of internal analytical precision using high-energy (A) and low-energy (B) paths. Dashed line denotes theoretical error predicted by Johnson−Nyquist noise and counting statistics; dotted line denotes unknown error of 0.01‰; red line denotes total predicted internal error. $\delta^{82/78}$Se data show near-optimal internal precision of individual analyses in both non-CRC and CRC measurement modes. Internal precision is typically better after double spike (DS) data reduction (white circles) than for only standard-sample bracketing (SSB) data reduction (blue circles). All CRC measurements were performed with (He−)N_2 gas mixture except subset denoted as using He−H_2.

And represents the effective counts of ions registered on the detectors for an isotope ratio measurement. Here n_a and n_b denote the ion counts observed by the detector for each isotope in an isotope ratio analysis, calculated from the recorded voltage (V_i) as $n_i = (t)(V_i)$ (cps V^{-1}) where t denotes the integration time (here 4 s × 50 cycles = 200 s) and cps V^{-1} denotes the conversion factor from volts to counts per second (cps), typically estimated as 62.5×10^6 for 10^{11} Ω resistors.

The internal precision of an isotope ratio measurement will be the sum of error contributions from Johnson–Nyquist noise, counting statistics, and any further contributions from unknown sources ($\sigma_{unknown}$):

$$\sigma_{internal} = \sqrt{\sigma_{Johnson}^2 + \sigma_{counting}^2 + \sigma_{unknown}^2} \quad (24)$$

We consider the internal precision as a function of Se introduced to the mass spectrometer, converting from n_{eff} assuming an uptake time of 467 μL min^{-1}, analysis time of 280 s, and signal transmission of 560 V per ppm. We found that in both CRC and non-CRC measurement modes, individual analyses show a trend of improving internal precision with greater Se introduction that follows the Johnson–Nyquist noise and counting statistics theoretical lines, with an inferred $\sigma_{unknown}$ contribution of ~0.01‰ (Fig. 5). This agrees with similar assessments made for other elements analyzed via MC-ICP-MS,[50–52] and confirms that under optimal tuning, measurement precision can be maximized in both CRC and non-CRC modes.

In addition to maximizing internal precision, we considered the reproducibility of replicate analyses. We did so using error-normalized deviates (END's),[50–52] with END calculated:

$$END = \frac{\delta Se_i - \delta Se_j}{\sqrt{\sigma_i^2 + \sigma_j^2}} \quad (25)$$

where δSe_i and δSe_j denote individual measurements of delta values on a sample solution, and σ_i and σ_j are their respective internal analytical errors. Replicate analyses that vary in proportion to their internal error alone will yield a population of END values with a standard deviation (σ_{END}) of unity. If $\sigma_{END} > 1$, it means that additional variance is generated between analyses. For data reduced only via standard-sample bracketing (SSB), we observed average σ_{END} values of ~2.6 for non-CRC analyses and ~1.5 for CRC analyses (Fig. 6); in both cases, σ_{END} was lower for double spike (DS) reduced data. We hypothesize that lower σ_{END} for CRC analyses derives from near-complete removal of Ar-based isobaric interferences, causing a greater proportion of variance to be driven by mass bias fluctuations, which can be corrected by the double spike (while fluctuations in isobaric interferences cannot). This improves the external reproducibility of analyses in CRC mode (discussed further below).

Finally, we assessed the accuracy and precision of our data using three-isotope plots for data reduced only via standard-sample bracketing (i.e., without double spike deconvolution). Our analyses fall within certified/published values[18,32,35,46] for the NIST standard and MH-495 (Fig. 3B), as well as SCo-1 ($\delta^{82/}$
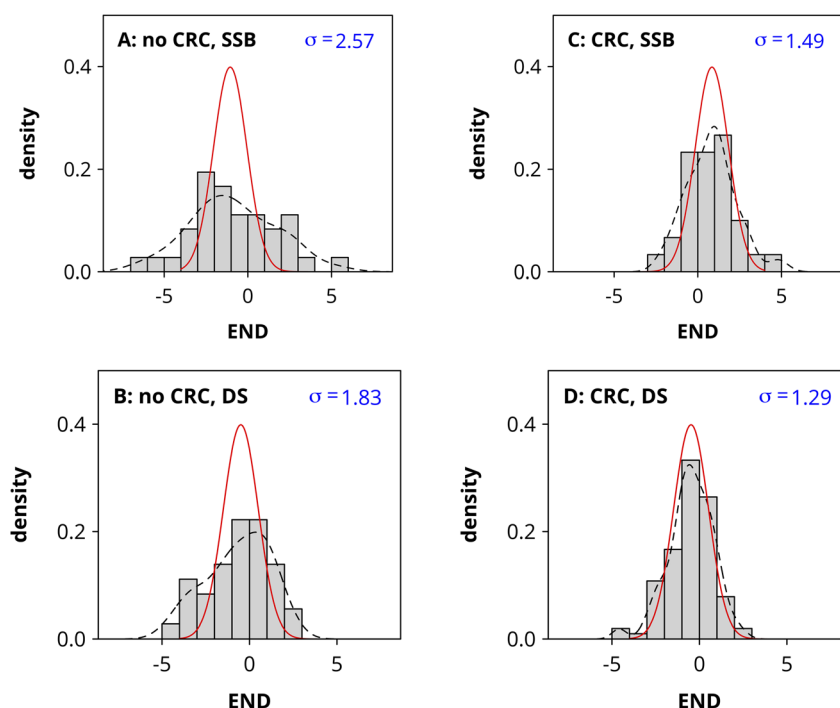

Fig. 6 Histograms of END's for (A and B) non-CRC and (C and D) CRC analyses. Red lines denote Gaussian distribution with $\sigma_{END} = 1$; dashed lines denote density of observed END values. In both non-CRC and CRC measurement modes, DS data reduction improves intermediate precision (σ_{END} approaches 1). CRC analyses are dominated by internal error, while non-CRC analyses have substantial additional uncertainty between replicate analyses. This difference is likely due to removal of interferences in CRC analyses, which cannot be corrected by the DS.

2798 | J. Anal. At. Spectrom., 2025, 40, 2792–2802

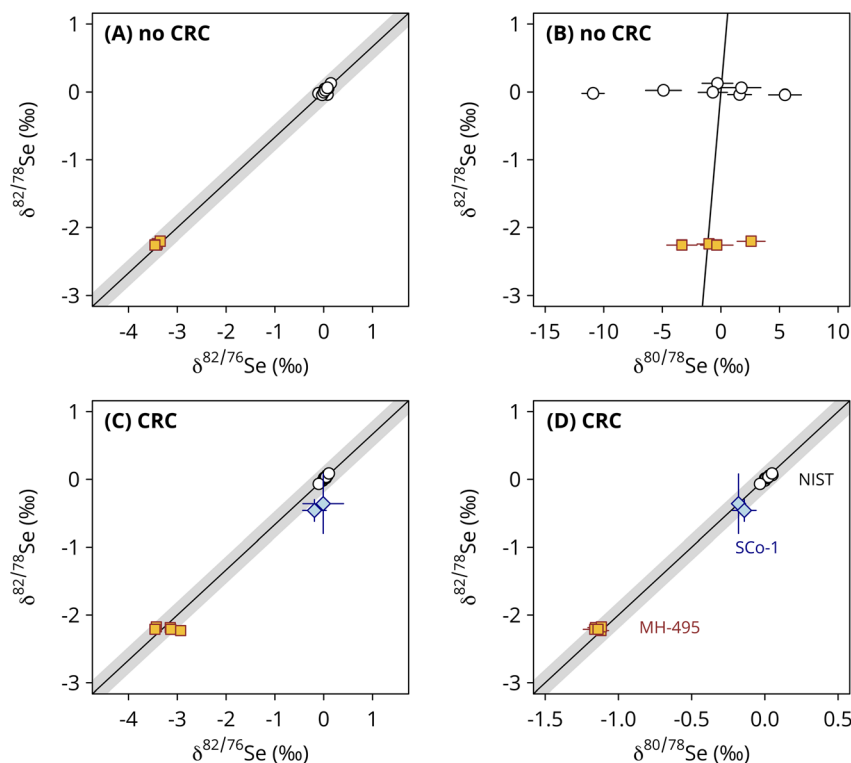This journal is © The Royal Society of Chemistry 2025

Fig. 7   Three isotope plots for (A and B) non-CRC and (C and D) CRC analyses. Mass-dependent fractionation is observed for all unspiked isotope pairs (i.e., excluding ^{74}Se and ^{77}Se), but $\delta^{80/78}$Se data show considerable scatter in non-CRC mode.

^{76}Se $= -0.10 \pm 0.24‰$, 2σ, $n = 6$) (Fig. 7). In non-CRC mode, mass-dependent fractionation (MDF) is observed for $\delta^{82/78}$Se vs. $\delta^{82/76}$Se, but not for $\delta^{80/78}$Se due to the imprecise correction for ^{80}ArAr interference (Fig. 7A). In contrast, CRC analyses show MDF patterns for both isotope pairs, reflecting effective ^{80}ArAr removal (Fig. 7B).

4.2   Sensitivity tests: molarity matching, concentration matching, Ge doping

After establishing our typical measurement conditions, we performed a range of tests to determine the sensitivity of Se isotopic analyses to suboptimal matching of samples and bracketing standards in terms of acid molarity, beam intensity,

and matrix element content. These tests were performed using both the high- and low-energy paths.

We first considered mismatch in HCl molarity between samples and bracketing standards. Typical analyses used 0.5 M HCl for sample and standard solutions, as well as the supplemental HCl in the HG. In these tests, the additional HCl of the HG was held at 0.5 M HCl and only the "sample" (NIST 3149) molarity was changed, to mimic sample dilution with incorrect acid concentration. In both the high- and low-energy paths, mismatch to 0.3 or 0.7 M HCl had a negligible impact on measured isotopic ratios (Fig. 8). In high-energy mode, mismatch to 0.1 or 0.9 M HCl was also negligible, but in low-energy mode these led to larger isotopic deviations for SSB
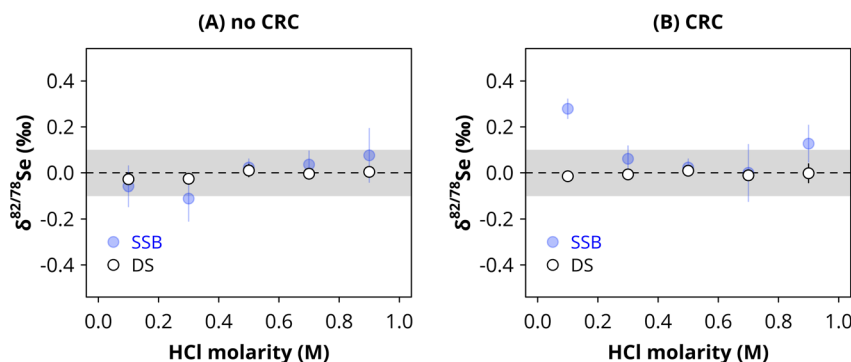

Fig. 8   Molarity matching tests for (A) non-CRC and (B) CRC analyses. Molarity mismatch of samples and standards causes only minor artifacts for SSB data and none for DS data.
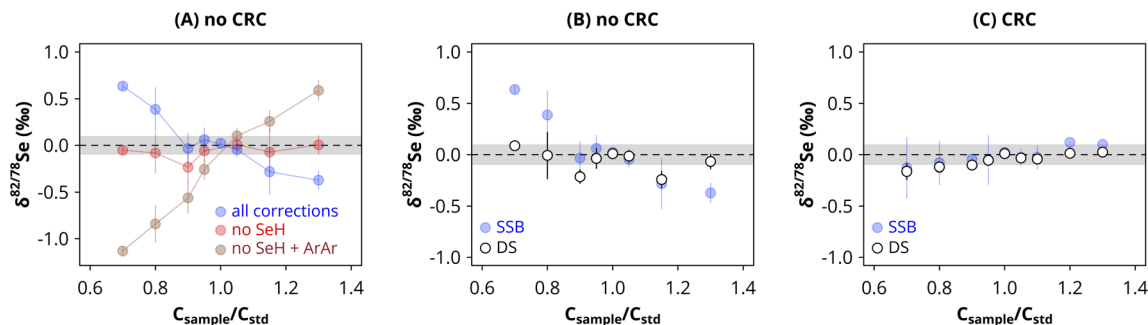
Fig. 9 Concentration matching tests. Large concentration mismatch effects are observed in non-CRC mode (A and B), but the magnitude and sign are affected by isobaric interference correction schemes (A) as well as tuning. Double spike data reduction corrects much of the mismatch effect (B). For CRC analyses (C), concentration mismatch effects are much smaller in both SSB and DS data.

data, while DS-reduced data remained unaffected (Fig. 8). While this reveals a greater sensitivity of CRC than non-CRC analyses to molarity matching, subtle differences between batches of 0.5 M HCl are unlikely to lead to isotopic artifacts in either measurement mode. We note that molarity matching sensitivity becomes greater when the SeH correction is not implemented, highlighting the importance of this step.

We next considered samples that are mismatched in Se concentration relative to bracketing standards. We explored this using NIST 3149 solutions that were 70% to 130% concentrated relative to bracketing 40 ppb NIST 3149 solutions. We observed a strong intensity-mismatch effect for SSB data in both high- and low-energy modes. In high-energy (non-CRC) mode, an effect of +0.05‰ per −3% intensity mismatch is observed for $\delta^{82/78}Se$ values determined by standard-sample bracketing (SSB, Fig. 9A and B). Given that our achievable external precision is <0.05‰, this means that a few percent concentration mismatch could have detectable effects. Careful, iterative dilution is therefore imperative to make high-precision Se isotopic analyses using SSB data reduction only for non-CRC analyses. However, we note a few qualifications to this statement.

First, the magnitude – and even sign – of intensity mismatch effect depends on the isobaric interference corrections that are implemented. The SeH correction is particularly sensitive to

intensity mismatch (Fig. 9A). Additionally, the magnitude of intensity mismatch effect varies between sessions, due to both tuning parameters and absolute measurement intensity. For all of these reasons, great care must be taken to produce high-precision Se isotope ratios *via* SSB data reduction. However, DS deconvolution successfully corrects for much of this effect (Fig. 9B), meaning that analyses only targeting mass-dependent fractionation patterns that implement DS data reduction are less susceptible to these analytical artifacts.

In contrast, we observe a much weaker intensity mismatch effect for CRC analyses (Fig. 9C), particularly when unnecessary isobaric interference corrections are eliminated. Due to the near-complete removal of ArAr dimers, ArAr and ArArH corrections can be omitted without consequence for measurement accuracy or precision. Thus, for CRC analyses, DS-reduced data show a weak intensity mismatch effect, meaning matching of standard and sample signals to within 10% is adequate to minimize analytical artifacts.

Last, we considered matrix contamination from Ge. While we employ Ge interference corrections as described in Section 2.5.5, these corrections are subject to uncertainty as the Ge signal becomes larger in magnitude. We find that in both non-CRC and CRC modes, Ge contamination up to Ge/Se = 1 does not significantly impact $\delta^{82/78}Se$ values measured *via* SSB (Fig. 10), as expected since there are no isobaric interferences

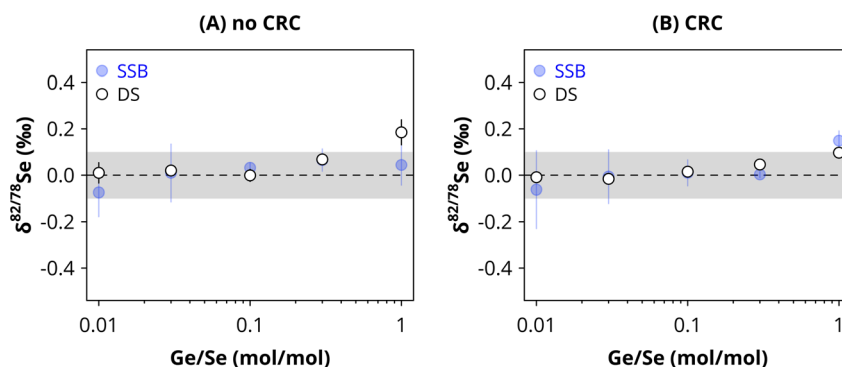**Fig. 10** Germanium doping tests for (A) non-CRC and (B) CRC analyses. Monitoring [73]Ge to correct contributions from [74]Ge and [76]Ge removes most artifacts up to Ge/Se ~1. At high Ge/Se, an accurate estimate of instrumental mass bias is critical and inaccuracies in these estimates create uncertainty in the data.

2800 | *J. Anal. At. Spectrom.*, 2025, **40**, 2792–2802

This journal is © The Royal Society of Chemistry 2025

from Ge on mass 78 or 82 (which is one of the reasons for reporting this ratio). Furthermore, DS-reduced data are robust up to Ge/Se = 0.1 and show only small (∼0.1‰) artifacts at Ge/Se = 1 (Fig. 10). This suggests that Ge correction *via* ^{73}Ge monitoring and mass bias inference from Se isotope fractionation is adequate to capture most realistic Ge contributions to the mass 74 and 76 signals that would arise from incomplete Ge removal during Se purification.

4.3 Outlook for Se isotopic analysis *via* CRC-MC-ICP-MS

We close by considering the outlook for the role of CRC-MC-ICP-MS in the future of Se isotope geochemistry. There are two main reasons that CRC-enabled Se isotope analysis has been of interest: (i) removing ArAr interferences to allow robust analysis of all Se isotopes for investigations of mass-independent behavior, (ii) reducing sample requirements, *e.g.* by allowing ^{80}Se analysis. To the first point, we have shown that assessments of MDF patterns are feasible at high precision, including for ^{80}Se, using CRC measurement mode on the Nu Sapphire (Fig. 7). This opens up the possibility of more precisely interrogating natural materials for the presence of mass-independent fractionation (MIF). While MIF has not been found in previous studies,[27,33,46] low-level effects might have escaped prior detection due to analytical uncertainty stemming from isobaric interference corrections in the absence of a collision–reaction cell.

As for sample requirements, we present here a brief assessment of the improvement in analytical precision when using the CRC. As noted above, with optimal tuning, maximum signal intensity can roughly be matched between non-CRC and CRC analyses of the same solutions. Thus, internal precision (*i.e.*, individual isotopic analyses), which is dictated by counting statistics and scales with the square root of effective ions counted (eqn (22)), is roughly equivalent for analysis of a given isotope ratio in non-CRC *vs.* CRC mode, using standard-sample bracketing.

We can also consider the addition of the ^{80}Se signal to the double spike deconvolution in CRC analyses. In a simplified case where each ratio used in the deconvolution contributes equally, the addition of ^{80}Se would bring the system from 4 to 5 equations, meaning internal error would scale from $\sqrt{1/4}$ to $\sqrt{1/5}$, implying an improvement of ∼11%. Considering that ^{80}Se is the most naturally abundant Se isotope and thus has greater signal intensity, this improvement of precision would be ∼16% assuming uniform relative standard errors on all isotope ratios. However, these simplified scenarios over-estimate the real improvement in internal precision because (i) measurement precision on individual isotope ratios does not scale directly with counts in all cases (some are "cleaner" than others due to lack of interferences), and (ii) all ratios are highly correlated, meaning the addition of ^{80}Se adds less constraint to the system than if it were an independent estimate. Using measured internal errors on individual isotope ratios, we infer that the inclusion of ^{80}Se in the deconvolution improves internal precision by no more than 3%.

Despite the lack of change in internal precision, significant improvement in the reproducibility of replicate analyses is observed in CRC mode (Fig. 6). A decrease of σ_{END} from 1.83 to 1.29 between non-CRC and CRC modes implies a ∼40% improvement in external reproducibility. Put another way, this means that CRC analyses can match the precision of non-CRC analyses using roughly half as much Se. We note that the magnitude of improvement in precision varies across sessions, but in almost all instances yields tens of percent reduction in sample requirement for CRC analyses. We attribute this improvement to the removal of Ar-based interferences, which are not perfectly corrected in non-CRC measurements.

Finally, we note that in addition to superior analytical precision, CRC analyses are less sensitive to concentration mismatch (Fig. 9). This means that imperfections in dilutions and evaporation during analysis will have smaller impacts on CRC data. Altogether, this points to CRC analysis as an attractive choice for Se isotope measurements due to the achievable precision and resilience to analytical conditions.

5. Conclusions

We have presented a method for precise Se isotopic analysis using a Nu Sapphire CRC-MC-ICP-MS. This method has the advantage of removing Ar-based interferences and thus enables precise and accurate analysis of all Se isotopes. This will open up the possibility of investigating low-magnitude mass-independent effects. Furthermore, the CRC analyses allow superior analytical precision per ng of Se analyzed, due to incorporation of the ^{80}Se signal in double spike deconvolution and the improved reproducibility of replicate analyses. These advances will be useful for the expansion of Se isotope studies into low-Se reservoirs.

Author contributions

Conceptualization: MAK, methodology: MAK, LP, DP, investigation: MAK, LP, supervision: MAK, funding acquisition: MAK, writing – original draft: MAK, writing – review & editing: MAK, LP, DP.

Conflicts of interest

There are no conflicts of interest to declare.

Data availability

The data supporting this article have been included in the main text, figures and tables.

Acknowledgements

This journal is © The Royal Society of Chemistry 2025

J. Anal. At. Spectrom., 2025, **40**, 2792–2802 | **2801**

References

1 V. M. Goldschmidt, *J. Chem. Soc.*, 1937, 655–673.

2 P. J. Harrison, P. W. Yu, P. A. Thompson, N. M. Price and D. J. Phillips, *Mar. Ecol.: Prog. Ser.*, 1988, 89–96.

3 U. Tinggi, *Toxicol. Lett.*, 2003, **137**, 103–110.

4 M. Petrović, *ChemTexts*, 2021, **7**, 11.

5 A. D. Lemly, *Ecotoxicol. Environ. Saf.*, 1997, **36**, 275–281.

6 T. S. Presser, D. Z. Piper, K. J. Bird, J. P. Skorupa, S. J. Hamilton, S. J. Detwiler and M. A. Huebner, in *Handbook of Exploration and Environmental Geochemistry*, Elsevier, 2004, vol. 8, pp. 299–319.

7 K. Mitchell, S. Z. Mansoor, P. R. D. Mason, T. M. Johnson and P. Van Cappellen, *Earth Planet. Sci. Lett.*, 2016, **441**, 178–187.

8 E. E. Stüeken, *Rev. Mineral. Geochem.*, 2017, **82**, 657–682.

9 E. E. Stüeken and M. A. Kipp, *Selenium Isotope Paleobiogeochemistry*, Cambridge University Press, 2020.

10 M. J. Herbel, T. M. Johnson, R. S. Oremland and T. D. Bullen, *Geochim. Cosmochim. Acta*, 2000, **64**, 3701–3709.

11 A. S. Ellis, T. M. Johnson, M. J. Herbel and T. D. Bullen, *Chem. Geol.*, 2003, **195**, 119–129.

12 K. Schilling, A. Basu, C. Wanner, R. A. Sanford, C. Pallud, T. M. Johnson and P. R. Mason, *Geochim. Cosmochim. Acta*, 2020, **276**, 274–288.

13 N. L. Wasserman, K. Schilling, T. M. Johnson and C. Pallud, *ACS Earth Space Chem.*, 2021, **5**, 1140–1149.

14 S. K. Clark and T. M. Johnson, *J. Environ. Qual.*, 2010, **39**, 2200–2210.

15 K. Schilling, T. M. Johnson and W. Wilcke, *Soil Sci. Soc. Am. J.*, 2011, **75**, 1354–1364.

16 K. Schilling, T. M. Johnson, K. S. Dhillon and P. R. D. Mason, *Environ. Sci. Technol.*, 2015, **49**, 9690–9698.

17 K. Mitchell, P. R. Mason, P. Van Cappellen, T. M. Johnson, B. C. Gill, J. D. Owens, J. Diaz, E. D. Ingall, G.-J. Reichart and T. W. Lyons, *Geochim. Cosmochim. Acta*, 2012, **89**, 302–317.

18 J.-M. Zhu, T. M. Johnson, S. K. Clark, X.-K. Zhu and X.-L. Wang, *Geochim. Cosmochim. Acta*, 2014, **126**, 228–249.

19 E. E. Stüeken, J. Foriel, R. Buick and S. D. Schoepfer, *Chem. Geol.*, 2015, **410**, 28–39.

20 P. A. P. von Strandmann, E. E. Stüeken, T. Elliott, S. W. Poulton, C. M. Dehler, D. E. Canfield and D. C. Catling, *Nat. Commun.*, 2015, **6**, 10157.

21 M. A. Kipp, E. E. Stüeken, A. Bekker and R. Buick, *Proc. Natl. Acad. Sci. U. S. A.*, 2017, **114**, 875–880.

22 M. C. Koehler, R. Buick, M. A. Kipp, E. E. Stüeken and J. Zaloumis, *Proc. Natl. Acad. Sci. U. S. A.*, 2018, **115**, 7711–7716.

23 A. Yierpan, S. König, J. Labidi and R. Schoenberg, *Sci. Adv.*, 2020, **6**, eabb6179.

24 O. Rouxel, Y. Fouquet and J. N. Ludden, *Geochim. Cosmochim. Acta*, 2004, **68**, 2295–2311.

25 A. Yierpan, S. König, J. Labidi and R. Schoenberg, *Geochim. Cosmochim. Acta*, 2019, **249**, 199–224.

26 A. Grosche, M. Keith, R. Klemd, H. Strauss, C. Rosca and S. König, *Geochim. Cosmochim. Acta*, 2024, **372**, 13–27.

27 J. Labidi, S. König, T. Kurzawa, A. Yierpan and R. Schoenberg, *Earth Planet. Sci. Lett.*, 2018, **481**, 212–222.

28 M. I. Varas-Reus, S. König, A. Yierpan, J.-P. Lorand and R. Schoenberg, *Nat. Geosci.*, 2019, **12**, 779–782.

29 S. R. Taylor and S. M. McLennan, *Rev. Geophys.*, 1995, **33**, 241–265.

30 R. L. Rudnick and S. Gao, *Treatise Geochem.*, 2003, **3**, 659.

31 G. A. Cutter and K. W. Bruland, *Limnol. Oceanogr.*, 1984, **29**, 1179–1192.

32 T. Kurzawa, S. König, J. Labidi, A. Yierpan and R. Schoenberg, *Chem. Geol.*, 2017, **466**, 219–228.

33 E. E. Stüeken, J. Foriel, B. K. Nelson, R. Buick and D. C. Catling, *J. Anal. At. Spectrom.*, 2013, **28**, 1734–1749.

34 M.-L. Pons, M.-A. Millet, G. N. Nowell, S. Misra and H. M. Williams, *J. Anal. At. Spectrom.*, 2020, **35**, 320–330.

35 O. Rouxel, J. Ludden, J. Carignan, L. Marin and Y. Fouquet, *Geochim. Cosmochim. Acta*, 2002, **66**, 3191–3199.

36 D. Layton-Matthews, M. I. Leybourne, J. M. Peter and S. D. Scott, *J. Anal. At. Spectrom.*, 2006, **21**, 41–49.

37 Y. Chang, J. Zhang, J.-Q. Qu and Y. Xue, *Chem. Geol.*, 2017, **471**, 65–73.

38 N. Elwaer and H. Hintelmann, *Anal. Bioanal. Chem.*, 2007, **389**, 1889–1899.

39 J. W. Olesik and P. J. Gray, *Spectrochim. Acta, Part B*, 2014, **100**, 197–210.

40 D. Peters and Y. Gérard, in *Goldschmidt 2023 Conference*, GOLDSCHMIDT, 2023.

41 J. F. Rudge, B. C. Reynolds and B. Bourdon, *Chem. Geol.*, 2009, **265**, 420–431.

42 M. Klaver and C. D. Coath, *Geostand. Geoanal. Res.*, 2019, **43**, 5–22.

43 S. G. John, *J. Anal. At. Spectrom.*, 2012, **27**, 2123–2131.

44 R. T. Marquez and F. L. Tissot, *Chem. Geol.*, 2022, **612**, 121095.

45 T. M. Johnson, M. J. Herbel, T. D. Bullen and P. T. Zawislanski, *Geochim. Cosmochim. Acta*, 1999, **63**, 2775–2783.

46 P. A. P. von Strandmann, C. D. Coath, D. C. Catling, S. W. Poulton and T. Elliott, *J. Anal. At. Spectrom.*, 2014, **29**, 1648–1659.

47 J. Wang, T. Ren, H. Lu, T. Zhou and M. Zhao, *Int. J. Mass Spectrom.*, 2011, **308**, 65–70.

48 D. M. R. Jones, *A study of ion-molecule reactions in a dynamic reaction cell to improve elemental analysis with inductively coupled plasma-mass spectrometry*, The Ohio State University, 2007.

49 N. Dauphas, A. Pourmand and F.-Z. Teng, *Chem. Geol.*, 2009, **267**, 175–184.

50 S. G. John and J. F. Adkins, *Mar. Chem.*, 2010, **119**, 65–76.

51 M. A. Kipp, H. Li, M. J. Ellwood, S. G. John, R. Middag, J. F. Adkins and F. L. Tissot, *Geochim. Cosmochim. Acta*, 2022, **336**, 231–248.

52 G. Paris, A. L. Sessions, A. V. Subhas and J. F. Adkins, *Chem. Geol.*, 2013, **345**, 50–61.

2802 | *J. Anal. At. Spectrom.*, 2025, **40**, 2792–2802

This journal is © The Royal Society of Chemistry 2025